Response of onshore oceanic heat supply to yearly changes in the Amundsen Sea icescape (Antarctica)

P. St-Laurent, S.E. Stammerjohn, T. Maksym

Accepted 4 March 2024 in J.Geophys.Res.Oceans, https://doi.org/10.1029/2023JC020467

Keypoints

- Ice shelves such as Crosson and Thwaites have multiple viable sources of oceanic heat helping to sustain their high melting rates
- The relative importance of these sources evolve in response to changes in icescape such as the collapse of the Thwaites Glacier Tongue
- The fast-ice cover seaward of Pine Island Glacier does not mitigate its high melting rates and has remote impacts reaching up to Crosson

Abstract

The heat transfer between the warm oceanic water and the floating portion of the Antarctic ice sheet (the ice shelves) occurs in a dynamic environment with year-to-year changes in the distribution of icebergs and fast-ice (the 'icescape'). Dramatic events such as the collapse of glacier tongues are apparent in satellite images but oceanographic observations are insufficient to capture the synoptic impact of such events on the supply of oceanic heat to ice shelves. This study uses a 3D numerical model and semi-idealized experiments to examine whether the current high melting rates of ice shelves in the Amundsen Sea could be mitigated by certain icescape configurations. Specifically, the experiments quantify the impacts on oceanic heat supply of presence/absence of the Thwaites Glacier Tongue, Bear Ridge Iceberg Chain, tabular iceberg B22, and fast-ice cover seaward of Pine Island Ice Shelf (PIS). The experiments reveal that future changes in the coastal icescape are unlikely to reverse the high ice shelf melting rates of the Amundsen Sea, and that icescape changes between 2011–2022 actually enhanced them slightly. Ice shelves such as Crosson and Thwaites are found to have multiple viable sources of oceanic heat whose relative importance may shift following icescape reconfigurations but the overall heat supply remains high. Similarly, the formation of a fast-ice cover seaward of PIS slows down the cavity circulation (by 7%) but does not reduce its heat supply.

Plain Language Summary

The Antarctic ice sheet is a gigantic volume of ice whose edges in certain locations are in direct contact with the ocean ('ice shelves'). A warm oceanic water mass is causing the ice shelves to melt faster which accelerates the flow of ice from the Antarctic continent to the ocean. This contributes to a slow but steady rise in sea level that threatens the sustainability of coastal communities (where a large fraction of the world's population lives). Preparing these communities for the future requires knowing how much sea level will rise and how fast. Our confidence in future sea level estimates is partly limited by the fact that ice shelf sizes and iceberg conditions change from one year to the next, leading to a complex, continuously evolving ice landscape ('icescape'). We examined whether certain icescape configurations could hinder the circulation of warm water and limit how much heat comes in contact with the ice shelves. The computer simulations suggest that the ocean can rapidly adapt its pathways around the changing icescape in such a way that melting rates remain high. This result removes a layer of uncertainty from our estimates of future sea level rise.

1 Introduction

The floating portion of the Antarctic ice sheet, the ice shelves, exhibit some of their highest melting rates in the Amundsen Sea *Rignot et al.* (2019) and have the potential to contribute to global sea level rise substantially over the next century (e.g., *Joughin et al.*, 2021). The connection between the high melting rates and the presence of a warm oceanic water mass (modified Circumpolar Deep Water, mCDW) has been established for some time (e.g.,

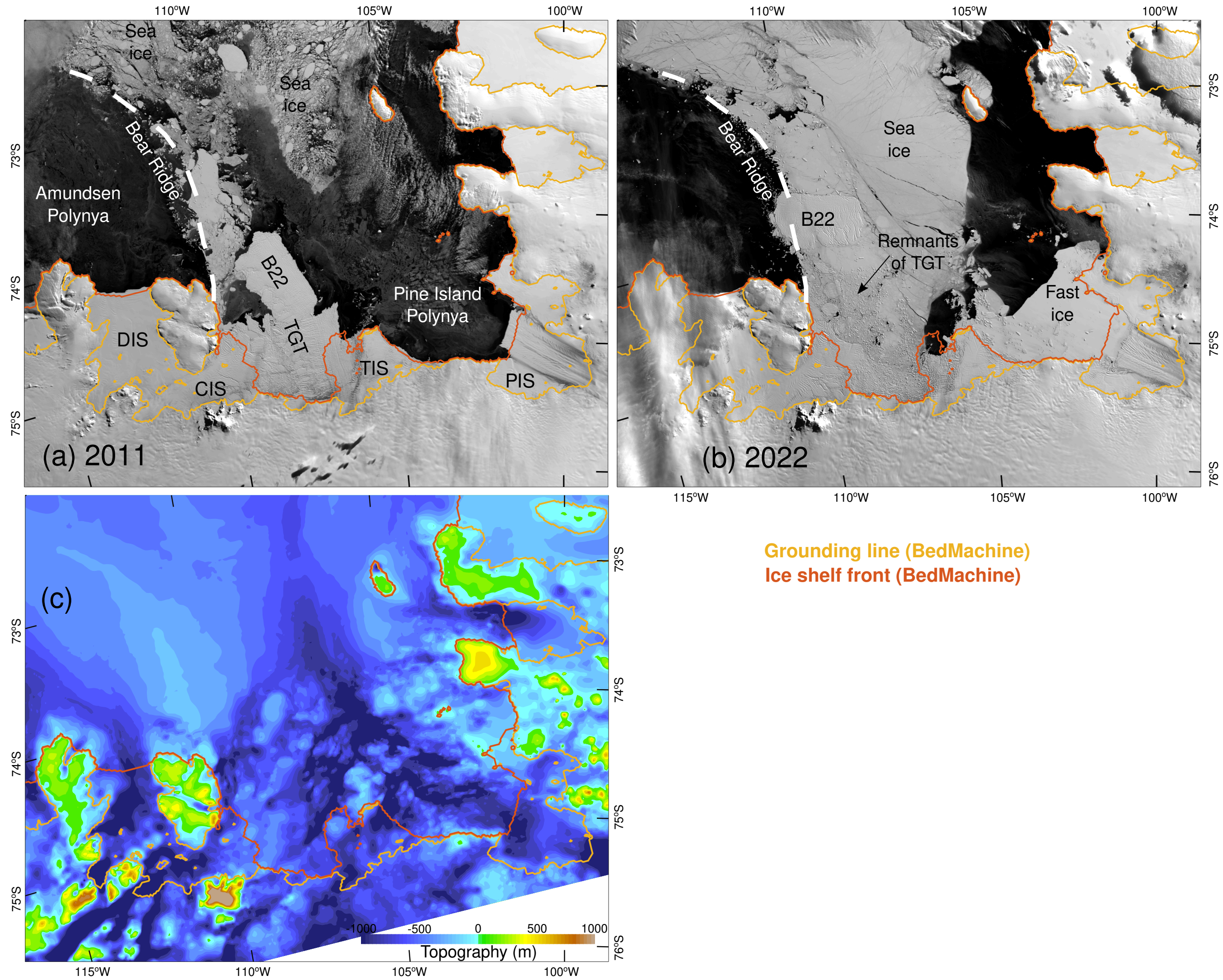

Figure 1: Contrast between two very different 'icescape' configurations in the eastern Amundsen Sea embayment. (a) Thwaites Glacier Tongue (TGT) at its maximum extent (9 March 2011 *Scambos et al.*, 2022). B22 is a tabular iceberg joined to the TGT on this date. (b) Complete breakup of the TGT into small individual icebergs, with a fast-ice cover between Thwaites Ice Shelf (TIS) and Pine Island Ice Shelf (PIS; 13 March 2022). Icebergs and ice shelves are distinguished from sea ice or fast-ice by their corrugated appearance. The dashed line represents Bear Ridge. DIS: Dotson Ice Shelf, CIS: Crosson Ice Shelf. (c) Topography of the study area. The grounding line and ice shelf front are from *Morlighem* (2020).

Pritchard et al., 2012) but this heat transfer from the ocean to ice shelves occurs in a dynamic environment. For example, the seaward extent of Thwaites Ice Shelf (TIS, Fig. 1) varied by ∼ 100 km over the years to periodically form the Thwaites Glacier Tongue (TGT; *MacGregor et al.*, 2012). This mass of floating glacial ice ebbed and flowed following glacier acceleration/deceleration (e.g., *Miles et al.*, 2020) and with the shedding of icebergs ('calving'). In particular, the large tabular iceberg B22, that calved from Thwaites in 2002 (*Stammerjohn et al.*, 2015), remained in the eastern Amundsen Sea until 2023. Its large size (82 × 44 km), combined with the proximity of the coast and of numerous smaller icebergs, contributed to heavy sea ice conditions between 107°W and 110°W during this period (Fig. 1).

Another feature contributing to the regional 'icescape' is Bear Ridge, a shallow (∼ 300 m deep) ridge extending seaward along 110°W from Bear Peninsula (Fig. 1). Icebergs become grounded along the ∼ 150 km-long ridge to form an 'iceberg chain' (*Macdonald et al.*, 2023; *Mazur et al.*, 2019; *Nakayama et al.*, 2014; *Bett et al.*, 2020) which we refer to as the Bear Ridge Iceberg Chain (BRIC). Fast-ice forms between the grounded icebergs so that sea ice is unable to drift westward with the dominant winds, allowing the formation of the Amundsen Sea Polynya (ASP; Fig. 1a). The BRIC and the ASP are apparent every year in passive microwave-derived sea ice concentrations for 2006–2022 (*Comiso*, 2017) and in visible satellite images for 2001–2022 (*Scambos et al.*, 2022), suggesting these are permanent features of the Amundsen Sea. The area between TIS and Pine island Ice Shelf (PIS) can also exhibit an extensive (~ 75 km-wide) fast-ice cover in some but not all years (it was present in eight out of 22 years between 2001–2022 (*Scambos et al.* (2022); see also Fig. 1b). At times, this fast-ice cover has remained in place for up to three years at a time (2004–2006) and therefore is not merely a seasonal feature.

These interannual variations in the Amundsen icescape have the potential to alter the supply of oceanic heat to ice shelves greatly. In contrast to the relatively mobile sea ice, fast-ice and ice shelves nearly completely shield the ocean from mechanical and thermodynamical exchanges with the atmosphere. The coastal oceanic circulation of the Amundsen is sensitive to this mechanical stress (*Yang et al.*, 2022; *Zheng et al.*, 2022; *Kim et al.*, 2021) and is thus expected to change in response to the formation/collapse of the TGT (or of the fast-ice near PIS). For example, *Dotto et al.* (2022) report an uplift of isotherms under TIS in response to the formation of the PIS fast-ice around 2021. Also, ice shelf fronts (and the icebergs shed from them) have very thick drafts $O(300\,\mathrm{m})$, i.e. comparable to the pycnocline depth in the Amundsen Sea (e.g., *Jacobs et al.*, 2012). When the TGT grows over the years, the surface oceanic circulation is forced to be re-directed around the growing obstacle, and away from the coast and the grounding zones. Fast-ice, glacial ice tongues, and grounded icebergs can also alter sea ice production simply by displacing polynyas or creating new ones. In turn, this production can affect the thermocline depth, a key parameter in determining basal melt rates (*De Rydt et al.*, 2014).

Given these considerations, we raise the question: could the high ice shelf melting rates currently observed in the Amundsen Sea be mitigated by certain icescape configurations? This question is the primary motivation for the present study, which aims at evaluating how regional changes in icescape might impact oceanic heat pathways and basal melt rates (e.g., *Cougnon et al.* (2017), in the context of the Mertz Glacier Tongue). Specifically, the study focuses on abrupt, year-to-year changes such as the collapse of the TGT between 2011 and 2013, or the periodic formation of the fast-ice cover near PIS. The study complements earlier efforts focused on the impact of iceberg chains and their melt on the Amundsen hydrography (*Nakayama et al.*, 2014; *Bett et al.*, 2020). Another question related to the Amundsen's icescape is how freely mCDW circulates under large tabular icebergs such as B22. From a dynamical perspective, an isolated tabular iceberg can be conceptualized as an inverted seamount. Depending on the vertical stratification, iceberg keel, and background flow, the presence of the iceberg can lead to partial/total blocking of the oceanic flow (Taylor columns; e.g., *Ou*, 1991). Here, partial/total blocking refers to the fluid from upstream being able to occupy a portion of the area under the iceberg (partial) or none of it (total blocking). Although iceberg melt does not contribute to sea level rise, whether blocking occurs or not under a tabular iceberg can drastically change its contribution to regional freshwater fluxes.

The study is structured as follows. The experimental plan used to highlight impacts of changes in icescape is described in the next section. It includes an evaluation of the numerical model used for these experiments against historical cryospheric/oceanic observations. The analyses presented in the subsequent sections focus on heat delivery to the ice shelves, the dynamical impact of fast-ice, polynya dynamics, and heat supply under tabular icebergs. A discussion of these results in the context of the literature and of ongoing sea level rise conclude the study.

2 Methods

The study examines the impact of changes in icescape configuration on the oceanic heat supply to the ice shelves of the eastern Amundsen Sea. A set of numerical experiments is used to represent two contrasted configurations of the Thwaites Glacier Tongue (TGT; year 2011 versus 2022) while preserving all other components of the simulation the same to facilitate the interpretation. Additional experiments are used to highlight the role of the Bear Ridge Iceberg Chain (BRIC) and that of the fast-ice cover near PIS. Note that although drifting sea ice could be considered a component of the regional 'icescape', we interpret icescape as the collection of fast-ice, ice shelves, and icebergs.

2.1 Numerical model

The numerical model is an implementation of the Regional Ocean Modeling System (ROMS, *Shchepetkin and McWilliams*, 2005) for the Amundsen Sea (~90–140°W, ~68–76°S; *St-Laurent*, 2023). The computational grid has a uniform mesh size of 1.5 km in the horizontal plane and 20 topography-following levels. For comparison, the first baroclinic Rossby radius of deformation is ~ 4.4 km on the continental shelf. The model includes a dynamic and thermodynamic sea ice module (*Budgell*, 2005) and thermodynamic ice shelves (*Dinniman et al.*, 2011). The implementation is similar to that of *St-Laurent et al.* (2017) but benefits from improvements: a slightly larger regional domain, recent ROMS codebase (6 April 2020), topographic refinements (*Dorschel et al.*, 2022; *Jordan et al.*, 2020; *Morlighem*, 2020), 3-hourly meteorological forcing from ERA5 (*Hersbach et al.*, 2020), tidal forcing for 10 constituents (*Padman et al.*, 2002), and 5 km-resolution oceanic boundary conditions from *Dinniman et al.* (2020).

The vertical coordinate of the model imposes restrictions on how abruptly topography is allowed to change from one horizontal grid cell to the next (e.g., *Shchepetkin and McWilliams*, 2003). This is addressed by numerically smoothing the seabed topography as well as the ice shelf (and iceberg) drafts (an approximation since in reality ice shelf fronts and recently calved icebergs are assumed to have vertical edges corresponding to very steep slopes). In this model implementation, ice shelf fronts and iceberg edges are allowed a slope of 0.08 which corresponds to a

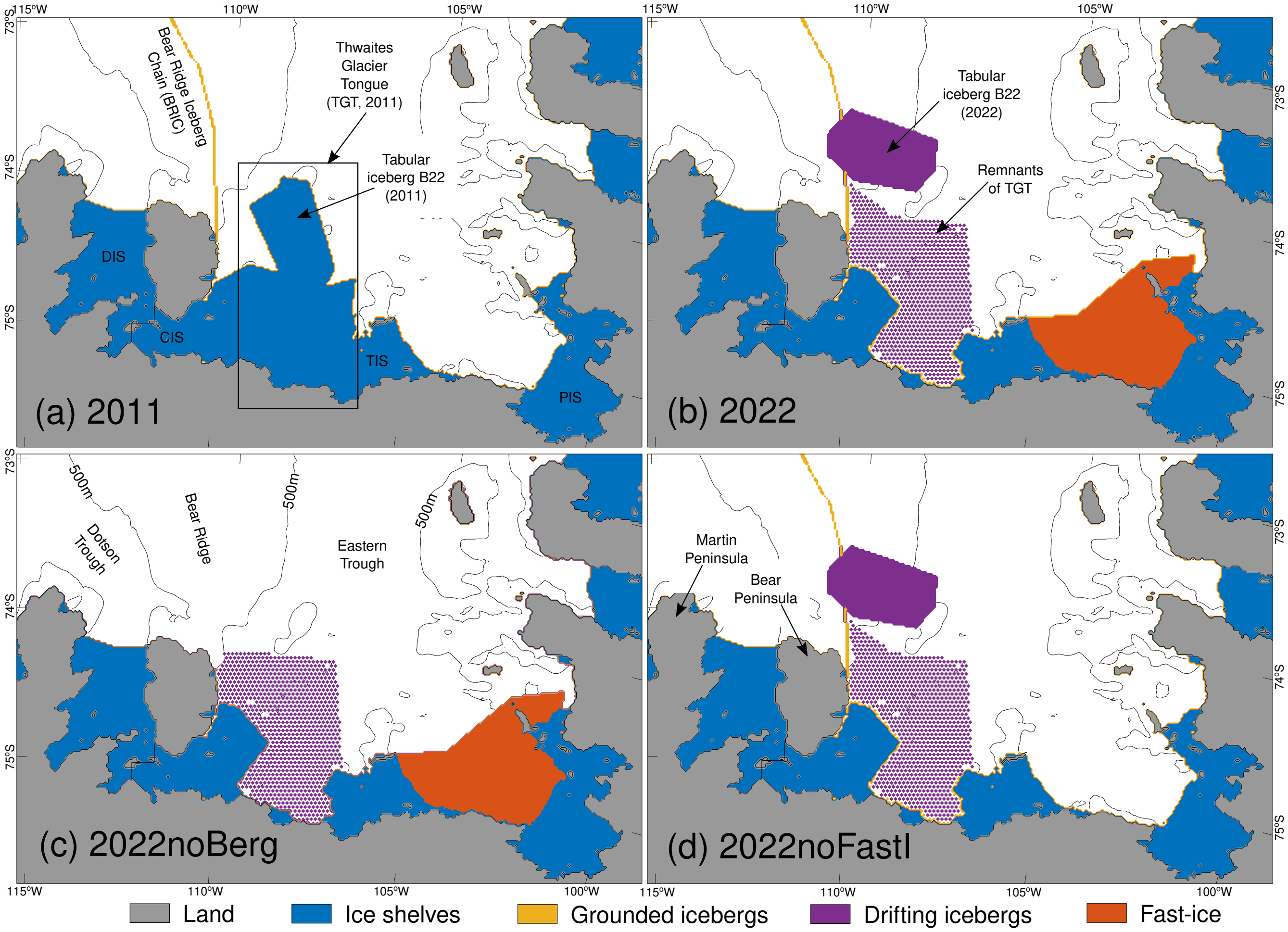

Figure 2: Geometry of the model experiments. (a) Year 2011, with key ice shelves labeled, (b) year 2022, (c) year 2022 without tabular iceberg B22 or the iceberg chain (2022noBerg), (d) year 2022 without fast-ice (2022noFastI). The key oceanographic and geographic features are highlighted in (c) and (d), respectively. The assumed boundary between Dotson Ice Shelf (DIS) and Crosson Ice Shelf (CIS) is represented in (a) and loosely based on *Rignot et al.* (2013). TIS: Thwaites Ice Shelf, PIS: Pine Island Ice Shelf.

vertical change of 120 m between two neighboring grid cells. Therefore, the transition between a 300 m-thick iceberg draft and open water would occur over ~ 3 grid cells. The physical consequence of this approximation is that the real potential vorticity gradient is underestimated by the model and that horizontal exchanges across this gradient could be overestimated. This is in contrast to geopotential-coordinate models that allow for arbitrarily-steep slopes while experiencing other well-documented limitations (e.g., *Gwyther et al.*, 2020).

2.2 Experimental plan

The numerical experiments of the study share the same initial condition (of 1 January 2010) taken from a realistic hindcast of 2006–2022 with a time-invariant icescape representative of year 2010 (*St-Laurent*, 2023). The January 2010 initial condition is modified to simulate four different icescapes mimicking conditions observed over the past 20 years (see below). Satellite images (*Scambos et al.*, 2022) indicate that such changes in icescape, like the break-up of the TGT or of the PIS fast-ice cover, often occur over periods of a few months to a year. The experiments thus have a duration of two years (1 Jan. 2010 to 31 Dec. 2011) where the first year (2010) is considered a “spin-up” allowing the ocean and sea ice to adjust themselves to the new icescape. For reference, the ‘flushing timescale’ of an Amundsen ice shelf cavity, computed as its volume divided by the volume of water circulating through it (~ 1 Sv, e.g., *Jourdain et al.*, 2017) is $O(1\,\text{month})$ and thus ice shelves adjust rapidly to changes in ambient conditions. All the analyses presented in the study are based on the second year of the experiments (2011). The possibility that the results could be sensitive to the time period (2010–2011) is investigated in additional experiments (see §2.3).

All four experiments share the same meteorology and lateral boundary conditions (edges of model domain) of 2010–2011 (even when the icescape represents year 2022) so that differences among the experiments are solely due to the icescapes. *Experiment 2011* represents the TGT at its maximum extent (Figs. 1a,2a). For CIS and TIS, the ice shelf draft of BedMachine is extended seaward assuming a fixed draft of 300 m to mimic the 2011 TGT. The BRIC, a chain of small individual icebergs grounded along Bear Ridge and interconnected with fast-ice, is represented in the model by a fixed surface obstacle with a thin draft of arbitrary value (0.1 m). While this value is thinner than typical fast ice, it allows the ocean to circulate unimpended (as the real ocean does in between the individual icebergs forming the BRIC) while at the same time preventing the westward drift of modeled sea ice (and thus allowing the formation of the Amundsen Sea Polynya; Fig. 1a). The TGT and the BRIC are represented in the model as ice shelves and have a fixed location and thickness over time. The ice shelves are assumed to be insulated from the atmosphere but they exchange heat and freshwater with the ocean based on local hydrodynamics and hydrographic conditions (*Dinniman et al.*, 2011). In the case of the BRIC, these exchanges are very small given its small surface area (Figs. 2a) and the fact that near-surface temperatures remain close to freezing except during the short austral summer. There is no attempt at representing the regional freshwater input from icebergs (e.g., *Bett et al.*, 2020) besides the TGT/BRIC parameterizations described above.

Experiment 2022 represents a collapsed TGT with the outline of the CIS and TIS mimicking satellite images (Figs. 1b,2b). Tabular iceberg B22 is now detached from the TIS and positioned northwest of its 2011 location. It has an assumed draft of 300 m (which allows for an oceanic flow underneath) and we neglect its drift over the period of the experiment (2 years). The numerous small drifting icebergs occupying the original location of the TGT are represented by a regular mesh of individual model grid points with fixed locations and an assumed draft of 0.1 m ("remnant of TGT"; Figs. 1b,2b). As before, the 0.1 m is an arbitrary value allowing for an unimpended oceanic circulation while modifying the modeled sea ice drift. The regular mesh limits the drift of modeled sea ice without completely blocking it and, overall, forms seasonal sea ice distributions consistent with satellite images (see §2.5). Year 2022 also exhibits an extensive and smooth region of ice cover between TIS and PIS (Figs. 1b,2b). This fast-ice is represented as an extension of TIS/PIS with an assumed draft of 0.1 m. The fast-ice prevents any mechanical forcing from winds and features a quadratic drag function of the ocean velocity at the ice/ocean interface. Although the fast-ice cover is allowed to exchange heat/freshwater with the ocean, its impact on the local hydrography is negligible compared to the thicker portions of the ice shelves that are positioned below the thermocline. Neither the fast-ice cover nor the remnant of the TGT are allowed to exchange fluxes with the atmosphere.

The purpose of *Experiment 2022noBerg* is to highlight the role of the BRIC and of tabular iceberg B22 by removing them from the 2022 icescape. Although satellite images going back to 2001 suggest that the BRIC is a permanent feature, the experiment clarifies how much the local ocean circulation and sea ice patterns owe to the presence of the BRIC, and what they could look like if changing wind patterns were to transport icebergs away from Bear Ridge. The PIS fast-ice and the TGT remnants remain in place although the latter is cropped at the northern edge of Bear Peninsula to allow for a free sea ice drift. *Experiment 2022noFastI* is identical to Experiment 2022 except for the absence of fast-ice in front of PIS so that its impact on the results can be evaluated. Note that this fast-ice gradually disappeared in the months following March 2022 (*Scambos et al.*, 2022) and that 2022noFastI is representative of conditions in early 2023.

The four experiments above are designed so that pair-wise comparisons between them highlight the contribution of specific icescape changes. For example, experiments 2011 and 2022noFastI both lack fast-ice in front of PIS, and the only thing distinguishing the two is the collapse of the TGT (Fig. 2a,d). By substracting the basal melt rate of experiment 2011 from that of 2022noFastI, one obtains the impact of this collapse on basal melt. Similarly, subtracting 2022noFastI from experiment 2022 provides the impact of the fast-ice in front of PIS (Fig. 2b,d). Subtracting experiment 2022 from 2022noBerg provides the impact of a hypothetical disappearance of the BRIC (Fig. 2a,c).

2.3 Sensitivity experiments

The set of experiments described above does not address the possibility that the impacts of icescape changes could vary depending on background hydrographic conditions. Observations from the Amundsen Sea (*Kim et al.*, 2021, their Fig. 8b) indicate that 2010–2011 was a relatively warm period followed by substantially cooler conditions in 2014–2015. To test the robustness of our conclusions regarding the impacts of icescape changes, we conduct four additional experiments identical to the ones described above except that: (1) the initial condition corresponds to 1 January 2014, and (2) the meteorology and lateral boundary conditions (edges of model domain) are for 2014–2015. This initial condition is taken from the same 2006–2022 hindcast (*St-Laurent*, 2023) that includes the warm/cool contrast (see Fig. S1). The four additional experiments are indentified with the suffix 'cold' to distinguish them from their 2010–2011 counterpart. For example, experiments '2011' and '2011_cold' share the same icescape configuration but differ in their hydrology/meteorology, and so on for the pairs '2022' and '2022_cold', '2022noBerg' and '2022noBerg_cold', '2022noFastI' and '2022noFastI_cold'.

An additional experiment (*2011FastI*, combining the ice shelf configuration of experiment 2011 and fast-ice in front of PIS) is conducted to evaluate the additivity of the oceanographic impacts of icescape changes between 2011 and 2022 (the latter including the TGT collapse and fast-ice in front of PIS; Fig. 2). Mathematical additivity would correspond to $impacts(TGT\,collapse + fast\,ice) = impacts(TGT\,collapse) + impacts(fast\,ice)$. The additivity is tested by comparing results from experiments (2022 − 2011) against those of (2022noFastI − 2011) + (2011FastI − 2011).

Any mismatch (nonlinearity) is interpreted as physical interactions arising when all icescape changes are present simultaneously.

2.4 Analyses: Horizontal oceanic fluxes of volume and heat

The model saves the daily-averaged 3D horizontal volumetric flux $\mathbf{Q}_{horiz}$ and potential temperature θ which are used to compute *a posteriori* the horizontal fluxes entering/leaving the ice shelf cavities. Note that the diurnal tidal constituents are the dominant ones in the Amundsen Sea and thus the daily average effectively filters tidal cycles (which are already fairly weak on the inner continental shelf; see *Jourdain et al.* (2019)). The heat flux is computed as $\rho_0\, c_p\, \mathbf{Q}_{horiz}\, (\theta - \theta_0)$ where $\rho_0 = 1028\,\mathrm{kg\,m^{-3}}$ is a reference value for seawater density, $c_p = 4 \times 10^3\,\mathrm{J}\,(\mathrm{kg\ K})^{-1}$ the specific heat, and $\theta_0 = -1.85°\mathrm{C}$ is a constant representative of the surface freezing temperature of seawater and of the 'Winter Water' layer occupying the upper $\sim 300\,\mathrm{m}$ of the water column (e.g., *Randall-Goodwin et al.*, 2015). This choice of θ_0 ensures that only mCDW contributes to the heat flux (e.g., *Jourdain et al.*, 2017).

For a given section such as the front of an ice shelf and for a given day of year 2011, the volume and heat fluxes perpendicular to the section are grouped into 'entering' or 'leaving' the ice shelf depending on the sign of the volumetric flux, and then they are averaged over the year 2011. The resulting decomposition reflects vertical and/or lateral variations in the horizontal flow perpendicular to the ice shelf front. The difference between the heat flux that enters or leaves an ice shelf cavity (i.e., the net heat flux) matches the ice shelf's 2011-averaged basal melt except for small variations in the cavity's heat content. Two-dimensional maps of the horizontal heat flux are also constructed by averaging this flux over year 2011 followed by a vertical summation over the 20 vertical levels.

2.5 Model-data comparisons

Daily sea ice concentrations at 25 km resolution from the Special Sensor Microwave/Imager (SSM/I) with the bootstrap algorithm (*Comiso*, 2017) are used to evaluate the modeled sea ice. Monthly averages of daily modeled/SSMI concentrations are computed around the first day of the months of 2011 and plotted side-by-side. The model simulates the key features of the seasonal cycle relatively well including the open water area in Feb.-Mar., the timing of polynya opening (Dec.) and that of sea ice growth (March; Fig. 3). Note the presence of three well-developed coastal polynyas in the January image (in both model and satellite): one next to Getz Ice Shelf (west of Siple Island), the Amundsen Sea Polynya, and the Pine Island Polynya. Relatively minor model biases include a high concentration bias over the Pine Island Polynya in Jan./Mar., a ASP that extends slightly too far north and west in Dec.-Feb., and a high concentration bias at the northern edge of the model domain in Dec.

Oceanographic data comprising 65 vertical profiles from the Amundsen Sea Polynya International Research Expedition (ASPIRE) collected between 13 December 2010 and 8 January 2011 (*Yager et al.*, 2012, 2016) are used to evaluate the modeled temperature and salinity in the Dotson area. The spatial coverage ranges from the shelf break ($\sim 71.5°$S) to the Dotson ice shelf front and from $\sim 119°$W to Bear Ridge. The model reproduces the characteristics of the Amundsen hydrography including the warm salty layer of mCDW at depth and the weak, quasi-linear haline stratification (see Fig. S4). Note that in the Amundsen Sea, salinity dictates the vertical density stratification and that sub-surface salinity and temperature both increase with depth (e.g., *Jacobs et al.*, 2012). Relatively small model biases include a 0.3°C warm bias centered around 200 m depth (i.e. in the 'Winter Water' layer) and a bias of +0.1 salinity units in the same layer.

A set of 106 hydrographic profiles from the eastern portion of the Amundsen Sea (72–90°S, 100–110°W, cruise NBP09-01 of Jan. 2009 to Feb. 2009) is used to evaluate the modeled temperature and salinity of that area. The model results for this evaluation are taken from the 2006–2022 hindcast of *St-Laurent* (2023). The model biases include a warm bias around 250 m depth reaching up to +0.5°C and a salty bias at a similar depth reaching up to +0.15 psu (Fig. S5). Note that this warm bias may originate from the high sea ice concentration bias noted earlier for the same area (which would in turn lead to insufficient winter ventilation of the upper 300 m) or from excessive vertical diffusivity. Biases in the rest of the water column are much smaller and amount to −0.25°C and −0.1 psu in the bottom layer (800 m depth).

Observational estimates of ice shelf basal melt rates representative of 2003–2008 (*Rignot et al.*, 2013) are used as a comparison point for the modeled results (Fig. S6). Although the time period and the icescape geometry are not a match for either of the 2011/2022 model configurations, the comparison indicates a broad agreement in the spatial distribution of basal melt as well as in their order of magnitude.

3 Results

This section focuses on four topics where changes in icescape were found to have a substantial impact: heat delivery to the ice shelves, the dynamical impact of fast-ice, polynya dynamics, and heat supply under tabular icebergs. The results are further discussed in the context of the literature and of ongoing sea level rise in the last section of the study.

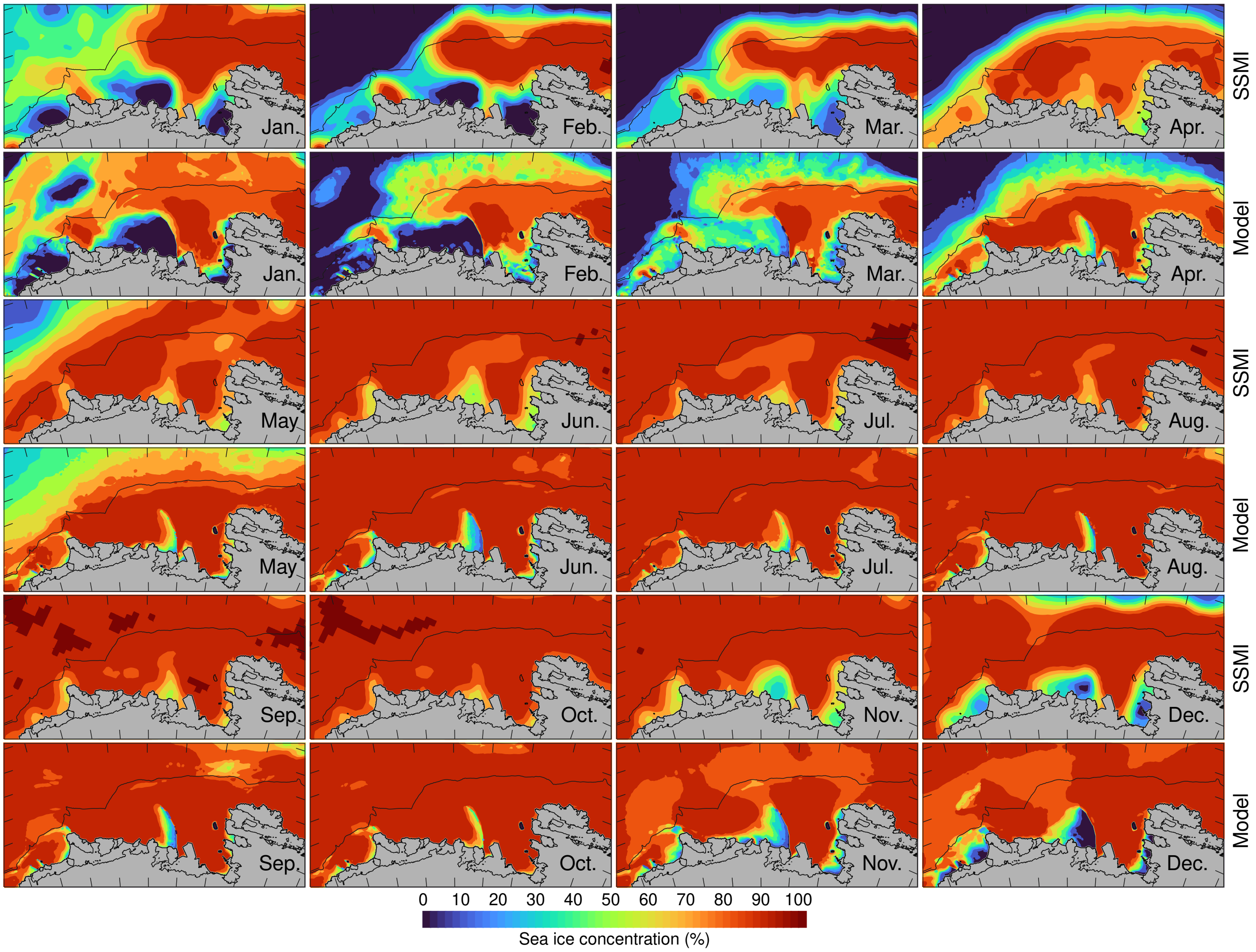

Figure 3: Comparison between sea ice concentration from satellite (SSM/I) and from experiment 2011. All fields are monthly averages centered around the first day of the month (1 Jan. 2011 to 1 Dec. 2011). The black horizontal line depicts the shelf break.

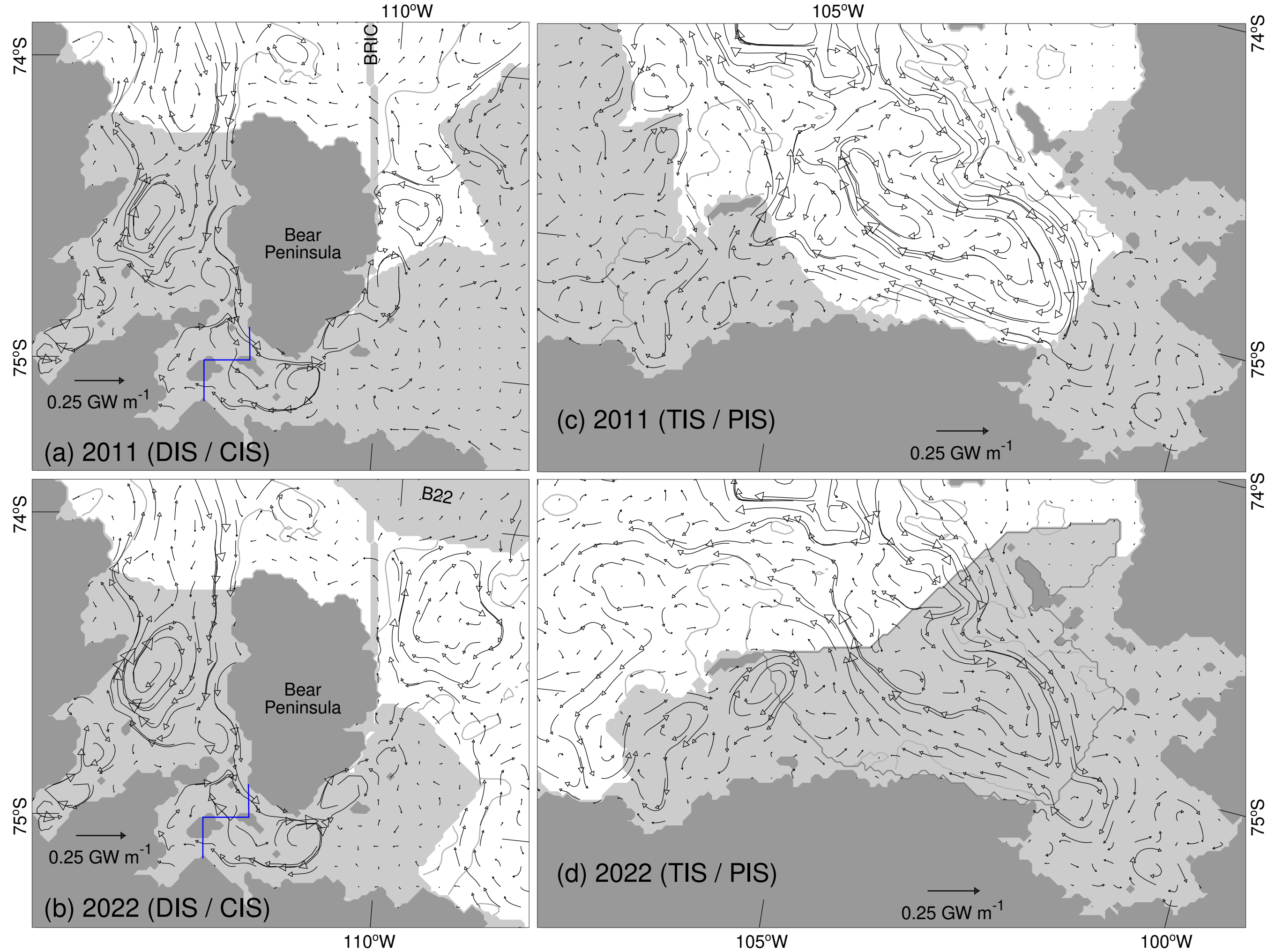

Figure 4: Horizontal oceanic heat flux in the vicinity of the ice shelves for two icescape configurations. (a) Heat flux near Dotson Ice Shelf (DIS) and Crosson Ice Shelf (CIS) in the 2011 and (b) 2022 configurations. (c,d) Same as a,b but for Thwaites Ice Shelf (TIS) and Pine Island Glacier Ice Shelf (PIS). The heat flux is vertically-integrated from the sea floor to the surface and averaged over the year 2011. Only one vector out of five is shown for clarity. The blue line is the assumed boundary between CIS and DIS. BRIC: Bear Ridge Iceberg Chain.

3.1 Supply of oceanic heat to the ice shelves

Basal melt under the ice shelves is associated with cyclonic (i.e., clockwise) circulations of volume and oceanic heat under DIS, CIS, TIS and PIS (Fig. 4). The cyclonic circulations form a two-way flow at the front of the ice shelves (i.e., entering/leaving the ice shelf) and at the boundary between DIS and CIS. In all cases, the two-way flow is an order of magnitude larger than the net flow across the ice shelf front and is $O(1\ \mathrm{Sv})$ for volume and $O(10\ \mathrm{TW})$ for heat (Table S1). In other words, the majority of the oceanic heat circulates in/out of the ice shelves without contributing to basal melt (e.g., *Jourdain et al.*, 2017).

A two-way flow at the ice shelf fronts remains in place in all four model experiments (Table S1) but the pathways of heat can change appreciably in response to changes in icescape. Northeast of Bear Peninsula, a number of gyres are apparent with their spatial extent and their center varying in response to the position of B22, which affects the heat flux arrows at the front of CIS (Fig. 4a,b). Specifically, the northward migration of B22 and the collapse of TGT lead to a $\approx 20\%$ weaker heat flux entering/leaving the front of CIS (compare experiments 2011 and 2022noFastI in Table S1). Between PIS and TIS, the presence of fast-ice leads to a weaker cyclonic gyre seaward of PIS and a 7% reduction in the volume flux of PIS (Fig. 4c,d, Table S1). For TIS, the presence of fast-ice to the east and the absence of TGT to the west in the 2022 icescape leads to a shift in the relative importance of the various inflows, with relatively more heat coming from the western side of TIS in 2022 than in 2011 (Fig. 4c,d). Specifically, the contribution from the segment west of 106.5°W increased from 24% in 2011 to 40% in the 2022 icescape following the collapse of the TGT.

The impact of these changes in heat pathways is reflected in the net heat flux (i.e. the sum of the two-way flow) across the ice shelf fronts and across the Dotson/Crosson boundary. In 2011, the net flux across the CIS front is

Table 1: Horizontal oceanic heat flux[a] and ice shelf basal melt[b] averaged over year 2011 in each icescape experiment

Horizontal oceanic heat flux (TW)					
Experiment	DIS	CIS	TIS	PIS	Do/Cr
2011	1.13	-0.03	0.75	0.93	-0.40
2022	0.89	0.40	0.99	1.01	-0.05
2022NoBerg	0.90	0.43	0.98	1.02	-0.02
2022NoFastI	1.01	0.23	0.85	0.97	-0.19
2011FastI	1.16	0.04	0.85	0.96	-0.36
Ice shelf basal melt (Gt yr^{-1})					
2011	68.6	34.1	69.7	89.6	
2022	76.6	42.2	83.2	96.3	
2022NoBerg	76.9	42.0	80.3	96.1	
2022NoFastI	72.7	38.3	71.2	91.6	
2011FastI	71.6	37.0	80.0	92.5	
Area (km^2)	5144	3479	2743	4750	
Volume (km^3)	2278	1211	1237	1418	

[a] The heat flux (see §2 for its equation and a definition of the acronyms) is integrated along the front of the ice shelf except for 'Do/Cr' where it is integrated along the boundary separating Dotson from Crosson; see Fig. 2a. The sign is positive when carrying heat into the ice shelf (and for 'Do/Cr', negative if flowing from Dotson to Crosson). See Table S1 for a decomposition of the flux into components entering/leaving the cavity.

[b] The ice shelf basal melt is horizontally integrated over the portion of the ice shelf common to all the experiments (with the area and cavity volume listed above).

$1\,\mathrm{Gt} = 10^{12}\,\mathrm{kg}$, $100\,\mathrm{Gt\,yr^{-1}} \Leftrightarrow 1.0584\,\mathrm{TW}$.

very weak (0.03 TW exiting the ice shelf) and CIS entirely depends on a 0.40 TW flux of heat coming from DIS in order to maintain its basal melt of 34.1 Gt yr^{-1} (Table 1). In the 2022 icescape, the heat flux across the CIS front increases by 0.43 TW, allowing for a 24% increase in the basal melt of CIS. At the same time, the heat transported from DIS to CIS decreases by 0.35 TW, indicating that CIS' heat source shifted between 2011 and 2022 from the DIS/CIS boundary to the front of CIS. The weakening of the exchanges between DIS and CIS in the 2022 icescape more than compensates for a reduction in the heat flux at the DIS front, with the melt of DIS increasing by 11% between 2011 and 2022 (Table 1).

Turning to TIS and PIS, experiments 2022 and 2022noFastI indicate that the collapse of the TGT and the presence of a fast-ice cover both contribute to increased heat supply to these ice shelves (Table 1). In the case of TIS, the collapse of the TGT (and the corresponding changes in pathways) is responsible for 0.10 TW out of the 0.24 TW increase in heat flux between 2011 and 2022 with the remainder due to the formation of the fast-ice cover (about 0.10 TW based on experiments 2011 and 2011FastI) and a small nonlinearity (0.04 TW). It is notable that the fast-ice has a positive effect on the heat supply despite insulating the nearby ocean from the wind forcing and causing drag against the surface circulation (a topic further examined in §3.2). The basal melt of PIS and TIS reflects the change in heat fluxes, with increases of 7–19% between 2011 and 2022. This increase in TIS' melt is primarily due to the fast-ice cover (+10.3 Gt yr^{-1} based on experiments 2011 and 2011FastI) and to a lesser extent to the TGT's collapse (+1.5 Gt yr^{-1} based on experiments 2011 and 2022noFastI; Table 1). The fourth experiment, 2022noBerg, yields heat fluxes and basal melt rates that are very similar to experiment 2022 (Table 1). It indicates that on year-to-year timescales, the formation/disappearance of the BRIC standing on top of the shallow Bear Ridge would have a fairly limited impact on the ice shelves' heat supply despite the BRIC playing a critical role in sea ice distributions (see §3.3). (Note that *Bett et al.* (2020) reported a qualitatively similar outcome from a comparable experiment.)

The additivity of the response to icescape changes can be evaluated from experiments 2011, 2011FastI, 2022noFastI and 2022 (see §2.3). The basal melt rates are always slightly higher when the icescape changes between 2011 and 2022 (TGT collapse and fast-ice) occur simultaneously by 11%, 12%, 13% and 27% for DIS, CIS, TIS, PIS, respectively (Table 1).

Repeating experiments 2011, 2022, 2022noBerg, and 2022noFastI in the cool oceanic conditions of 2015 leads to a general decrease in basal melt rates across icescape configurations and across individual ice shelves (between 8 and 18 Gt yr^{-1}; compare Tables 1 and S2). However, the impact of icescape changes on heat fluxes and basal melt rates, which corresponds to pair-wise differences between experiments having different icescape geometry but the same hydrography, is fairly similar under 'warm' or 'cold' conditions (see Fig. S7) since pair-wise differences are not affected by a ∼uniform offset in basal melt rates. The sign and the order of magnitude of the oceanographic response to icescape changes are similar for the hydrography of 2011 or 2015 (Fig. S7). For example, the addition of PIS's fast-ice (isolated from experiments 2022 and 2022NoFastI) increases the basal melt of TIS by +12.0 Gt yr^{-1} in the

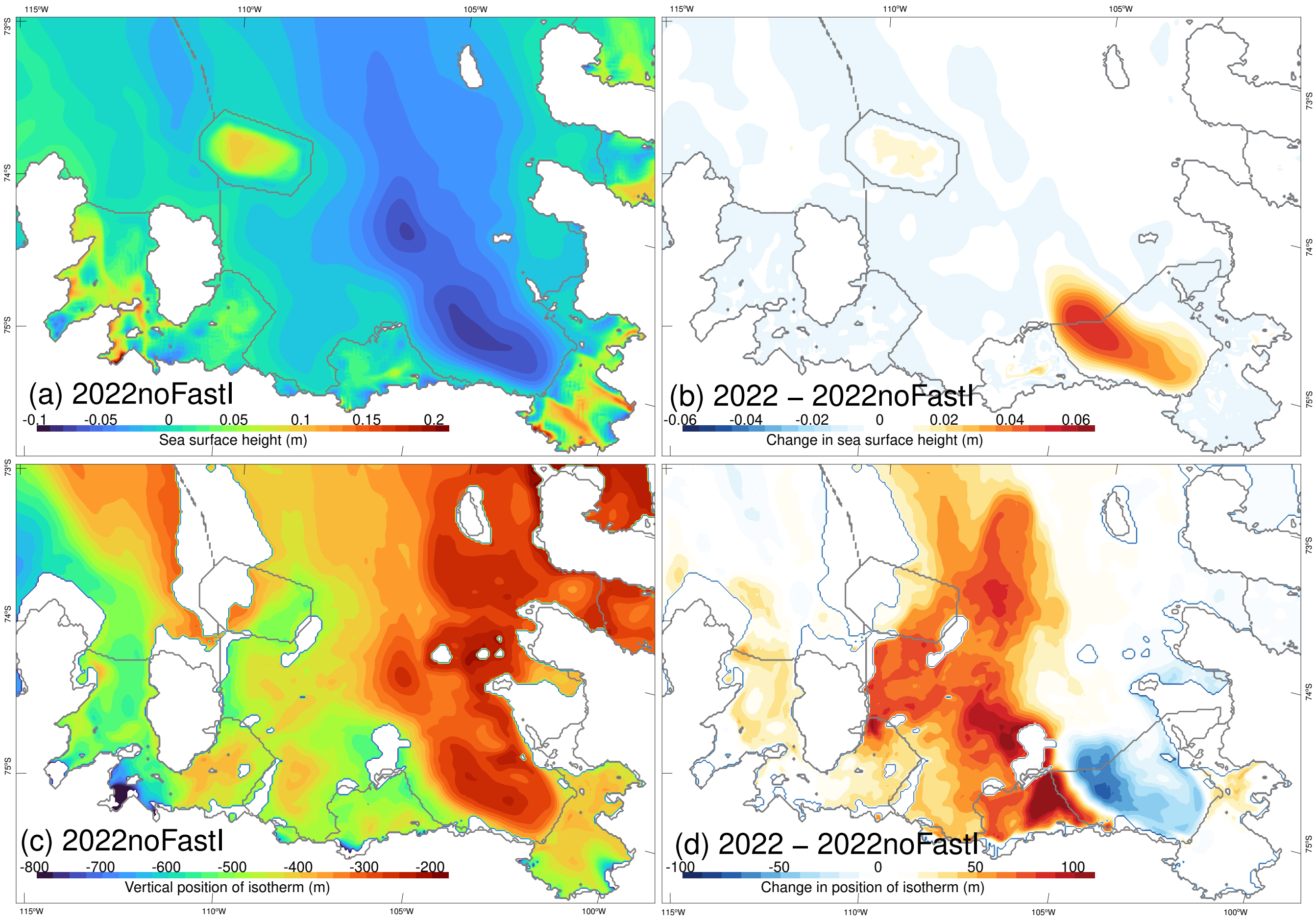

Figure 5: Impact of the fast-ice cover on the circulation and hydrography. (a) Sea surface height of experiment 2022noFastI. (b) Change in sea surface height due to the fast-ice cover. (c) Vertical position of the 0°C isotherm in experiment 2022noFastI (values increase upward; this particular isotherm is representative of the thermocline). White areas correspond to land and/or isotherm outcrops. (d) Change in the position of the isotherm due to the fast-ice cover. All fields are averaged over year 2011.

warm conditions of 2011 and by $+13.4$ Gt yr^{-1} in the cool conditions of 2015 (Tables 1 and S2). Overall, the impact of icescape changes appears to be robust across hydrographic conditions.

3.2 Fast-ice and its impact on the heat supply

The presence of a fast-ice cover between TIS and PIS was shown to increase heat fluxes and basal melt in the eastern Amundsen Sea (§3.1). This result may reflect a thermodynamic role played by fast-ice, e.g. where it insulates the ocean from the cold atmosphere during the winter, or a dynamic role related to changes in the surface stress experienced by the ocean. Comparisons between experiments 2022noFastI and 2022 reveal *lower* sub-surface temperatures seaward of PIS when fast-ice shields the ocean (not shown). Moreover, sea ice production in the eastern Amundsen Sea is either similar or slightly higher when the fast-ice is present (not shown). These results suggest a predominantly dynamical cause for the increase in basal melt. As noted in §3.1, the area west of PIS features a vigorous cyclonic circulation (gyre) corresponding to a local depression in the sea surface (Fig. 5a; see also *Thurnherr et al.* (2014) for direct observations of the gyre). The introduction of the fast-ice cover shields the ocean from the wind forcing and causes an appreciable slow down of the cyclonic gyre; the deceleration amounts to a flattening of the sea surface by up to 5 cm at the gyre's center (Fig. 5b).

In absence of the fast-ice cover, the baroclinic structure of the cyclonic gyre corresponds to a dome with elevated isopycnals/isotherms at the center and depressed isopycnals/isotherms at the periphery (Fig. 5c, as expected for horizontal velocity profiles weakening with depth). When the fast-ice cover is introduced, the dome flattens and the peripheral isotherms are raised by 50–75 m, which is the baroclinic response to the gyre's spin-down (Fig. 5d; note that this is the same dynamical process as reported by *Dotto et al.* (2022)). This shoaling of the isotherms occurs over a large portion of the eastern Amundsen embayment that includes TIS, CIS and DIS, and it directly impacts their thermal forcing given the quasi-linear thermal stratification of the region (see §2.5). Between experiments

2022noFastI and 2022, the basal melt of CIS increases by 10%, exemplifying the remote impact of the gyre's spin-down on the thermal forcing (Table 1). The shoaling of the isotherms impacts TIS the most (Fig. 5d) with a corresponding increase of 17% in its basal melt (Table 1).

3.3 Sea ice growth in polynyas after changes in icescape

Yearly changes in the Amundsen icescape have the potential to modify surface heat exchanges and sea ice growth substantially. This is examined by horizontally averaging the ocean surface fluxes over the central (110–120°W, 72–75°S, area of 8.78×10^4 km^2) and eastern (100–110°W, 72–75°S, area of 9.23×10^4 km^2) Amundsen continental shelf. These two areas are representative of the Amundsen and Pine Island polynyas (respectively). The averaging assumes a flux of zero under ice shelves, icebergs, and PIS' fast-ice, to specifically reflect exchanges between ocean and atmosphere/sea-ice. Note that in general, the wintertime variability of the surface heat flux mostly reflects fluctuations in the polynyas' extent and meteorology rather than surface oceanic temperatures (which are always confined to a narrow range of a few °C).

Experiment 2011 exhibits oceanic warming in January, neutral values in December/February, and cooling over the rest of the year (Fig. 6a,b). Sea ice melt is concentrated in January–February (i.e. a few months following the opening of the polynyas) while sea ice growth can occur anywhere from March to November (Fig. 6c,d). Only minor differences are apparent between experiments 2011 and 2022, which indicates that regionally-averaged fluxes are primarily set by the meteorology (which is the same in both experiments) and that the collapse of the TGT has a minor impact on sea ice growth in the polynyas (Fig. 6; growth is typically concentrated along the eastern edge of the two regions). Similarly, temperature conditions in the central Amundsen are largely unaffected by icescape changes taking place east of the BRIC (compare experiments 2011 and 2022 in Fig. 6e). In the eastern Amundsen, however, a small +0.1°C warming is apparent in the bottom layer between experiments 2011 and 2022 (Fig. 6f) primarily due to the fast-ice near PIS (§3.2).

The removal of the BRIC (experiment 2022noBerg) has a major impact on sea ice distributions and in turn the surfaces fluxes. Without this barrier, sea ice growth in the central region entirely depends on winds having a southerly component (i.e. directed offshore) to generate open water and large sea ice growth (compare Figs. 3, 7 and S10). Sea ice growth in the central region thus decreases by 53% in experiment 2022noBerg and the surface heat flux decreases by 27% (values averaged over year 2011; Fig. 6). Turning to the eastern region, the absence of the BRIC allows newly-produced sea ice to be continuously evacuated by the dominant easterly winds. Sea ice growth in this area thus increases by 30% between experiments 2011 and 2022noBerg, but this increase offsets only ∼half of the decrease occurring in the central region. (Similar outcomes were reported by *Nakayama et al.* (2014); *Bett et al.* (2020) for a comparable experiment.) Overall, experiment 2022noBerg suggests that the disappearance of the BRIC would change the spatial distribution of sea ice production and decrease its magnitude substantially over the Amundsen shelf as a whole. On the other hand, these substantial changes in sea ice do not affect the heat supply appreciably (§3.1, Table 1). The largest impact on oceanic temperatures is apparent in the central Amundsen where the signature of the cold winter mixed layer becomes subdued (Fig. 6e) following the reduction in polynya extent.

The same analyses conducted with the meteorology and hydrography of 2015 (cool conditions; §2.3) lead to the same outcomes (Fig. S8). Sea ice growth in the central region decreases by 58% in experiment 2022noBerg_cold and the surface heat flux decreases by 24% (values averaged over year 2015). In the eastern region, sea ice growth increases by 35% between experiments 2011_cold and 2022noBerg_cold. Overall, the impact of icescape changes on polynya fluxes appears to be robust across meteorologic and hydrographic conditions.

3.4 Circulation and melt under a tabular iceberg (B22)

The circulation of oceanic heat around tabular iceberg B22 is examined in the icescape configuration of 2022 (i.e., when B22 is independent from the TGT). Given the weak ambient stratification (Rossby radius of ∼ 4.4 km) and the assumed iceberg keel of 300 m (see §2), and based on the two-layer model of *Ou* (1991), one expects partial blocking in the top layer and a bottom layer that is either not blocked or only partially blocked. The 3D model of this study suggests that mCDW flows northward along the eastern edge of Bear Peninsula and then crosses iceberg B22 from one side to the other while supplying it with warm water (∼ 0.05°C; Fig. 8a,b). Such an unimpended flow in the bottom layer is confirmed by contours of potential vorticity $f/h = f\left(-\partial\rho_{pot}/\partial z\right)/\Delta\rho$ (with f the Coriolis parameter, h the layer's thickness, ρ_{pot} seawater potential density, z pointing upward, and $\Delta\rho$ an arbitrary constant) being continuous in and out of B22 for a layer representative of mCDW (1027.60 kg m^{-3}; not shown).

The situation reverses in the shallower layers where blocking becomes more apparent. In a layer representative of conditions just below B22 (1027.34 kg m^{-3}, Fig. 8b), the flow upstream of B22 splits upon reaching the iceberg and is nearly everywhere tangential to B22's outline (Fig. 8c). In the iceberg's inner region, the flow is dominated by an anticyclonic (i.e., counterclockwise) circulation that is most vigorous at the edges of B22. It is unclear to what extent the anticyclonic cell reflects a Taylor column or a melt-driven circulation, and it is worth pointing out that the edge of the iceberg is where the model dynamics are most likely to be affected by the vertical coordinate (see §2.1

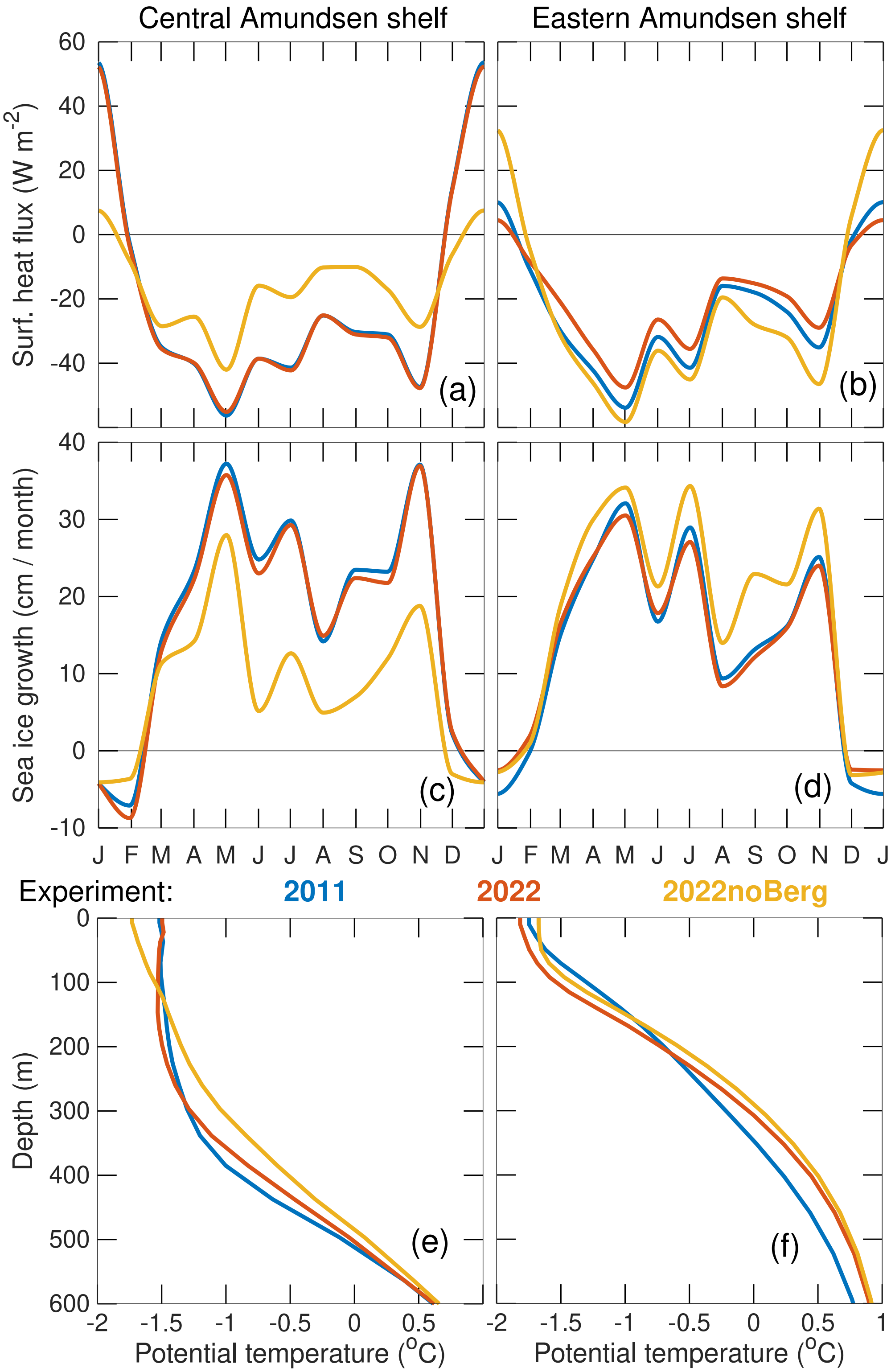

Figure 6: Surface fluxes horizontally-averaged over the central/eastern Amundsen continental shelf and oceanic temperature profiles (year 2011). The central and eastern regions are defined as 110–120°W,72–75°S and 100–110°W,72–75°S (respectively) and loosely correspond to the Amundsen Sea Polynya and Pine Island Polynya. In (a,b), the heat flux is defined positive if warming the ocean. In (c,d), negative sea ice growth represents sea ice melt. (e,f) Temperature profiles are from locations representative of the two polynyas (73°S,115°W and 74.25°S,105°W, respectively) and averaged over year 2011.

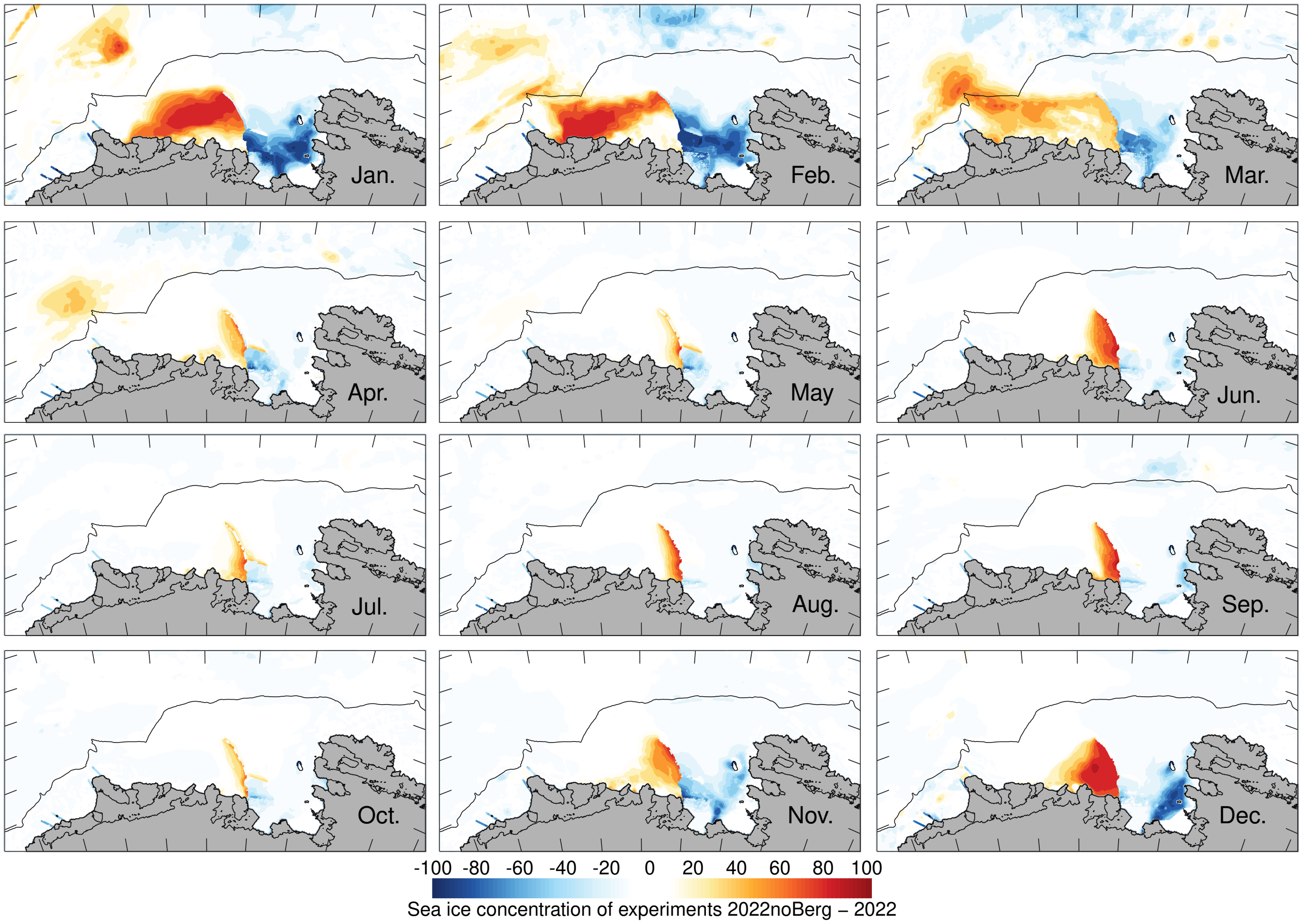

Figure 7: Differences in modeled sea ice concentration between experiments 2022noBerg and 2022. All fields are monthly averages centered around the first day of the month (1 Jan. 2011 to 1 Dec. 2011). The black horizontal line depicts the shelf break. See Fig. S10 for the absolute sea ice concentrations of experiment 2022noBerg.

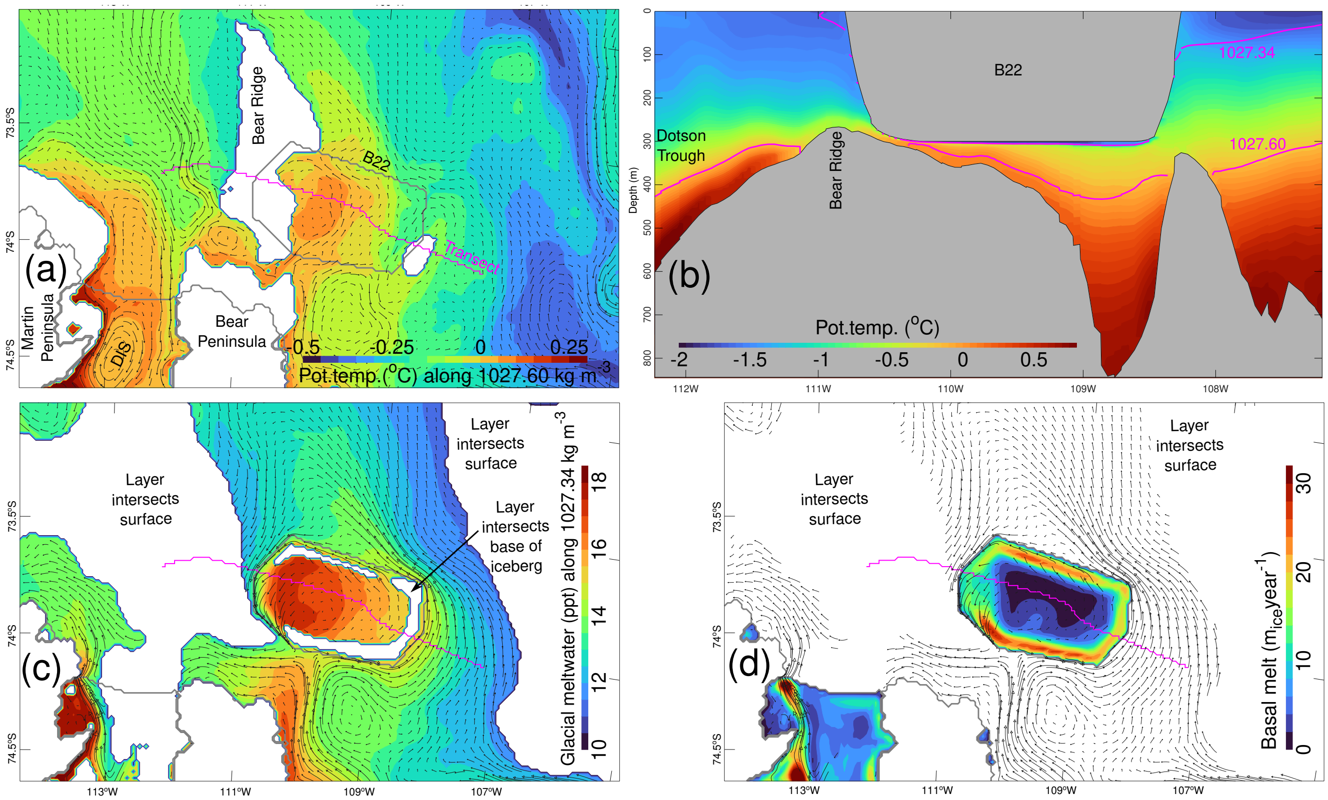

Figure 8: Physical conditions around tabular iceberg B22 in experiment 2022. (a) Potential temperature and oceanic flow for a layer representative of mCDW underneath B22 (1027.60 kg m^{-3}, ~350 m depth). The magenta line represents the transect of figure b. (b) Transect along the length of B22 with potential temperature and the position of layers 1027.34 and 1027.60 kg m^3. (c) Circulation and glacial meltwater for a layer grazing the bottom of B22 (1027.34 kg m^{-3}). (d) Basal melt rate and circulation along 1027.34 kg m^{-3}. All fields are averaged over year 2011.

and the Discussion). The melting rates under B22 reach up to 25 m of ice per year and are generally concentrated along the edges of the iceberg where flow velocities are the strongest (Fig. 8d). Glacial meltwater concentrations (estimated from modeled salinity and potential temperature following *Jenkins et al.* (2018)) thus reach up to 17 ppt in the iceberg's inner region (Fig. 8c). In spite of the anticyclonic circulation, some of the meltwater appears to escape B22 at its southwest corner and to ultimately join the meltwater outflow from CIS (Fig. 8c). Overall, the horizontally-integrated melt of B22 amounts to 30.7 Gt yr^{-1} on average over year 2011.

4 Discussion

The key outcome of the study (based on the finite number of experiments conducted) is that changes in the coastal icescape are unlikely to reverse or even mitigate the high ice shelf melting rates of the Amundsen Sea. Basal melt rates remain high in all the experiments and even increase after the formation of a fast-ice cover next to PIS (§3.1–3.2). Although lower melt rates occur in the 2011 icescape configuration (Table 1), the changes between the 2011/2022 configurations are smaller than those seen in multi-decadal simulations with time-invariant icescapes (*Naughten et al.*, 2022; *St-Laurent et al.*, 2022) or in interannual field campaigns (*Jenkins et al.*, 2018). The same conclusion is obtained in two different time periods (2010–2011 and 2014–2015) with substantially different hydrographic conditions and different meteorology. What becomes apparent from §3.1 is that ice shelves such as TIS or CIS have multiple viable pathways for heat supply. Recent fieldwork supports this view that ice shelves may have multiple sources of warm deep water (see Fig. 6 of *Wåhlin et al.* (2021) in the case of TIS, and *Girton et al.* (2019) for CIS). The available data also do not refute the possibility that the sources' relative importance could shift over the years to accommodate major changes in icescape (such as the presence/absence of the TGT; §3.1), in such a way that the high melting rates we currently experience (*Rignot et al.*, 2019) can continue unabated.

An icescape modification of a different type was considered by *Bett et al.* (2020) whereas a surface freshwater flux is prescribed near the coast to mimic iceberg melt. As in the present study, this addition did not reverse the high ice shelf melting rates, but actually increased bottom water temperatures on the shelf. *Bett et al.* (2020) attributed this result to weaker wintertime oceanic cooling in presence of the stabilizing surface buoyancy input. Overall, these results do not support the idea that changes in the Amundsen's icebergs/fast-ice would slow down the melt of ice shelves. Reversing the current high melting rates appears to require a change in the regional wind regime in order to, e.g., slow down the onshelf flux of mCDW (e.g., *Silvano et al.*, 2022; *Thoma et al.*, 2008), or enhance wintertime oceanic cooling upstream of ice shelves (*Bett et al.*, 2020; *Webber et al.*, 2017). This being said, the present study does not cover all the possible types of icescape changes. Other perturbations that took place in recent years include a retreat of the ice front of PIS (see *Yoon et al.*, 2022; *Bradley et al.*, 2022, 2023) and changes in the grounding zone of TIS (see *Milillo et al.*, 2019; *Holland et al.*, 2023). Future extreme icescape changes of such types (which were not explored in this study) could possibly lead to a reduction in ice shelf basal melt rates.

The study of *Dotto et al.* (2022) provides observational support for the substantial increase (+17%) in TIS' basal melt between experiments 2022noFastI and 2022 (§3.2). However, the present study suggests that the footprint of the gyre extends beyond TIS, and reaches as far as CIS and DIS (§3.2). This model result, along with the substantial throughflow between DIS and CIS (see §3.1, and the observations of *Girton et al.* (2019)) overall suggest that ice shelf cavities influence each other to a certain extent. Such remote connections can only be captured in regional models or with simultaneous measurements across regions of the Amundsen Sea (e.g., *Azaneu et al.*, 2023).

The unimpended flow of mCDW under B22 (§3.4) suggests that a surface obstacle is less constraining for mCDW than a bottom obstacle such as Bear Ridge (that divides mCDW into two geographical regions; see Fig. 1a of *Dutrieux et al.* (2014)). It also suggests a continuous supply of heat to the iceberg while it remains within the limits of the Amundsen continental shelf. Although the freshwater input associated with iceberg melt in the Amundsen remains uncertain and a topic of active research (e.g., *Tournadre et al.*, 2016), the 30.7 Gt yr^{-1} contribution of B22 (§3.4) amounts to as much as one third of that of TIS even though the latter exhibits basal melt rates $> 100\ \text{m}_{ice}\ \text{yr}^{-1}$ near the grounding zone (Fig. S6). The model may exaggerate the melt of B22 since the highest rates occur at the transition between the horizontal base and the vertical walls of the iceberg (Fig. 8) which only approximates the true geometry (see §2.1). The basal melt rates of iceberg B22 and the behavior of the shallow layer (1027.34 kg m^{-3}, Fig. 8) are therefore uncertain. For comparisons, *Jenkins* (1999) suggests heat fluxes of 150–300 W m^{-2} (equivalent to 15–30 $\text{m}_{ice}\ \text{yr}^{-1}$) under icebergs which would correspond to the high end of Fig. 8d. Iceberg models also indicate that on the scale of the Southern Ocean, wave erosion (not represented here) is a larger mass sink than basal melt, but at the same time, the influence of the former decreases in high sea ice conditions typical of continental shelves (see *Martin and Adcroft*, 2010). With a basal melt of 30.7 Gt yr^{-1}, B22 by itself would be contributing to as much as 4% of the global iceberg basal melt estimated at ~ 700 Gt yr^{-1} by *Martin and Adcroft* (2010). On the other hand, the large area of B22 is a rarity in Antarctic iceberg size distributions (*Tournadre et al.*, 2016) and its ultimate fate was to drift offshelf rather than to melt locally. Overall, the magnitude of the freshwater input from icebergs in the Amundsen Sea remains a substantial uncertainty.

Open Research Section

The model results supporting the conclusions are publicly available from *St-Laurent et al.* (2024). The ROMS computer code and input files are publicly available from *St-Laurent* (2023). ERA5 reanalyses were obtained from *Hersbach et al.* (2023). Hydrographic observations from ASPIRE were obtained from *Yager and Sherrell* (2019) and hydrographic observations from cruise NBP09-01 were obtained from *Boyer et al.* (2018).

Acknowledgments

This research was supported by NASA (award 80NSSC21K0746, Antarctic sea ice, fast ice and icebergs: Modulators of ocean-ice shelf interactions (AMICUS)) and by NSF (collaborative awards 1941292, 1941327). We thank M.S.Dinniman (Old Dominion University) for providing 5 km-resolution circumpolar model outputs for lateral oceanic boundary conditions as well as for helpful advice. The authors acknowledge William & Mary Research Computing (https://www.wm.edu/it/rc) for providing computational resources and/or technical support that have contributed to the results reported within this study. We thank the referees for their careful reading of the manuscript and for providing helpful and thoughtful comments.

References

Azaneu, M., B. Webber, K. J. Heywood, K. M. Assmann, T. S. Dotto, and E. P. Abrahamsen (2023), Influence of shelf break processes on the transport of warm waters onto the eastern Amundsen Sea continental shelf, *J. Geophys. Res. Oceans*, *128*(e2022JC019535), doi:10.1029/2022JC019535.

Bett, D. T., P. R. Holland, A. C. N. Garabato, A. Jenkins, P. Dutrieux, S. Kimura, and A. Fleming (2020), The impact of the Amundsen Sea freshwater balance on ocean melting of the west Antarctic ice sheet, *J. Geophys. Res. Oceans*, *125*(e2020JC016305), doi:10.1029/2020JC016305.

Boyer, T. P., O. K. Baranova, C. Coleman, H. E. Garcia, A. Grodsky, R. A. Locarnini, A. V. Mishonov, C. R. Paver, J. R. Reagan, D. Seidov, I. V. Smolyar, K. Weathers, and M. M. Zweng (2018), World Ocean Database 2018.

Bradley, A. T., D. T. Bett, P. Dutrieux, J. De Rydt, and P. R. Holland (2022), The influence of Pine Island ice shelf calving on basal melting, *J. Geophys. Res. Oceans*, *127*(e2022JC018621), doi:10.1029/2022JC018621.

Bradley, A. T., J. De Rydt, D. T. Bett, P. Dutrieux, and P. R. Holland (2023), The ice dynamic and melting response of Pine Island ice shelf to calving, *Annals of Glaciology*, *63*(87-89), 111–115, doi:10.1017/aog.2023.24.

Budgell, W. P. (2005), Numerical simulation of ice-ocean variability in the Barents Sea region: Towards dynamical downscaling, *Ocean Dyn.*, *55*, 370–387, doi:10.1007/s10236-005-0008-3.

Comiso, J. C. (2017), Bootstrap sea ice concentrations from Nimbus-7 SMMR and DMSP SSM/I-SSMIS, version 3 (2010–2011 used), Boulder, Colorado USA. NASA National Snow and Ice Data Center Distributed Active Archive Center, accessed 11 February 2022, doi:10.5067/7Q8HCCWS4I0R.

Cougnon, E. A., B. K. Galton-Fenzi, A. D. Fraser, and J. R. Hunter (2017), Regional changes in icescape impact shelf circulation and basal melting, *Geophysical Research Letters*, *44*, 11,519–11,527, doi:10.1002/2017GL074943.

De Rydt, J., P. R. Holland, P. Dutrieux, and A. Jenkins (2014), Geometric and oceanographic controls on melting beneath Pine Island Glacier, *J. Geophys. Res. Oceans*, *119*, 2420–2438, doi:10.1002/2013JC009513.

Dinniman, M. S., J. M. Klinck, and W. O. Smith Jr. (2011), A model study of Circumpolar Deep Water on the west Antarctic Peninsula and Ross Sea continental shelves, *Deep Sea Res. II*, *58*, 1508–1523, doi:10.1016/j.dsr2.2010.11.013.

Dinniman, M. S., P. St-Laurent, K. R. Arrigo, E. E. Hofmann, and G. L. van Dijken (2020), Analysis of iron sources in Antarctic continental shelf waters, *J. Geophys. Res.: Oceans*, *125*(e2019JC015736), doi:10.1029/2019JC015736.

Dorschel, B., L. Hehemann, S. Viquerat, F. Warnke, S. Dreutter, Y. S. Tenberge, D. Accettella, L. An, F. Barrios, E. Bazhenova, J. Black, F. Bohoyo, C. Davey, L. D. Santis, C. E. Dotti, A. C. Fremand, P. T. Fretwell, J. A. Gales, J. Gao, L. Gasperini, J. S. Greenbaum, J. H. Jencks, K. Hogan, J. K. Hong, M. Jakobsson, L. Jensen, J. Kool, S. Larin, R. D. Larter, G. Leitchenkov, B. Loubrieu, K. Mackay, L. Mayer, R. Millan, M. Morlighem, F. Navidad, F. O. Nitsche, Y. Nogi, C. Pertuisot, A. L. Post, H. D. Pritchard, A. Purser, M. Rebesco, E. Rignot, J. L. Roberts, M. Rovere, I. Ryzhov, C. Sauli, T. Schmitt, A. Silvano, J. Smith, H. Snaith, A. J. Tate, K. Tinto, P. Vandenbossche, P. Weatherall, P. Wintersteller, C. Yang, T. Zhang, and J. E. Arndt (2022), The International Bathymetric Chart of the Southern Ocean version 2, *Scientific Data*, *9*, doi:10.1038/s41597-022-01366-7.

Dotto, T. S., K. J. Heywood, R. A. Hall, T. A. Scambos, Y. Zheng, Y. Nakayama, S. Hyogo, T. Snow, A. K. Wåhlin, C. Wild, M. Truffer, A. Muto, K. E. Alley, L. Boehme, G. A. Bortolotto, S. W. Tyler, and E. Pettit (2022), Ocean variability beneath Thwaites eastern ice shelf driven by the Pine Island bay gyre strength, *Nature Communications*, *13*(7840), doi:10.1038/s41467-022-35499-5.

Dutrieux, P., J. De Rydt, A. Jenkins, P. R. Holland, H. K. Ha, S. H. Lee, E. J. Steig, Q. Ding, E. P. Abrahamsen, and M. Schroder (2014), Strong sensitivity of Pine Island ice-shelf melting to climatic variability, *Science*, *343*(174), 174–178, doi:10.1126/science.1244341.

Girton, J. B., K. Christianson, J. Dunlap, P. Dutrieux, J. Gobat, C. Lee, and L. Rainville (2019), Buoyancy-adjusting profiling floats for exploration of heat transport, melt rates, and mixing in the ocean cavities under floating ice shelves, *Oceans 2019 MTS/IEEE Seattle*, pp. 1–6, doi:10.23919/OCEANS40490.2019.8962744.

Gwyther, D. E., K. Kusahara, X. S. Asay-Davis, M. S. Dinniman, and B. K. Galton-Fenzi (2020), Vertical processes and resolution impact ice shelf basal melting: A multi-model study, *Ocean Modelling*, *147*, doi:10.1016/j.ocemod.2020.101569.

Hersbach, H., B. Bell, P. Berrisford, S. Hirahara, A. Horńyi, J. Munoz-Sabater, J. Nicolas, C. Peubey, R. Radu, D. Schepers, A. Simmons, C. Soci, S. Abdalla, X. Abellan, G. Balsamo, P. Bechtold, G. Biavati, J. Bidlot, M. Bonavita, C. G. De P. Dahlgren, D. Dee, M. Diamantakis, R. Dragani, J. Flemming, R. Forbes, M. Fuentes, A. Geer, L. Haimberger, S. Healy, R. J. Hogan, E. Hólm, M. Janisková, S. Keeley, P. Laloyaux, P. Lopez, C. Lupu, G. Radnoti, R. P. de I. Rozum, F. Vamborg, S. Villaume, and J.-N. Thépaut (2020), The ERA5 global reanalysis, *Q J R Meteorol Soc.*, *146*, 1999–2049, doi:10.1002/qj.3803.

Hersbach, H., B. Bell, P. Berrisford, G. Biavati, A. Horanyi, J. M. Sabater, J. Nicolas, C. Peubey, R. Radu, I. Rozum, D. Schepers, A. Simmons, C. Soci, D. Dee, and J. N. Thepaut (2023), ERA5 hourly data on single levels from 1940 to present, doi:10.24381/cds.adbb2d47.

Holland, P. R., S. L. Bevan, and A. J. Luckman (2023), Strong ocean melting feedback during the recent retreat of Thwaites glacier, *Geophys. Res. Lett.*, *50*(e2023GL103088), doi:10.1029/2023GL103088.

Jacobs, S., A. Jenkins, H. Hellmer, C. Giulivi, F. Nitsche, B. Huber, and R. Guerrero (2012), The Amundsen Sea and the Antarctic Ice Sheet, *Oceanography*, *25*(3), 154–163, doi:10.5670/oceanog.2012.90.

Jenkins, A. (1999), The impact of melting ice on ocean waters, *J. Phys. Oceanogr.*, *29*, 2370–2381.

Jenkins, A., D. Shoosmith, P. Dutrieux, S. Jacobs, T. W. Kim, S. H. Lee, H. K. Ha, and S. Stammerjohn (2018), West Antarctic Ice Sheet retreat in the Amundsen Sea driven by decadal oceanic variability, *Nature Geoscience*, *11*, 733–738, doi:10.1038/s41561-018-0207-4.

Jordan, T. A., D. Porter, K. Tinto, R. Millan, A. Muto, K. Hogan, R. D. Larter, A. G. C. Graham, and J. D. Paden (2020), New gravity-derived bathymetry for the Thwaites, Crosson, and Dotson ice shelves revealing two ice shelf populations, *The Cryosphere*, *14*, doi:10.5194/tc-14-2869-2020.

Joughin, I., D. Shapero, P. Dutrieux, and B. Smith (2021), Ocean-induced melt volume directly paces ice loss from Pine Island Glacier, *Science Advances*, *7*(eabi5738), doi:10.1126/sciadv.abi5738.

Jourdain, N. C., P. Mathiot, N. Merino, G. Durand, J. L. Sommer, P. Spence, P. Dutrieux, and G. Madec (2017), Ocean circulation and sea-ice thinning induced by melting ice shelves in the Amundsen Sea, *J. Geophys. Res. Oceans*, *122*, 2550–2573, doi:10.1002/2016JC012509.

Jourdain, N. C., J. M. Molines, J. L. Sommer, P. Mathiot, J. Chanut, C. de Lavergne, and G. Madec (2019), Simulating or prescribing the influence of tides on the Amundsen Sea ice shelves, *Ocean Modelling*, *133*, 44–55, doi:10.1016/j.ocemod.2018.11.001.

Kim, T. W., H. W. Yang, P. Dutrieux, A. K. Wåhlin, A. Jenkins, Y. G. Kim, H. K. Ha, C. S. Kim, K. H. Cho, T. Park, J. Park, S. Lee, and Y. K. Cho (2021), Interannual variation of modified Circumpolar Deep Water in the Dotson-Getz Trough, west Antarctica, *J. Geophys. Res.: Oceans*, *126*(e2021JC017491), doi:10.1029/2021JC017491.

Macdonald, G. J., S. F. Ackley, A. M. Mestas-Nunez, and A. Blanco-Cabanillas (2023), Evolution of the dynamics, area, and ice production of the Amundsen Sea Polynya, Antarctica, 2016–2021, *The Cryosphere*, *17*, 457–476, doi:10.5194/tc-17-457-2023.

MacGregor, J. A., G. A. Catania, M. S. Markowski, and A. G. Andrews (2012), Widespread rifting and retreat of ice-shelf margins in the eastern Amundsen Sea Embayment between 1972 and 2011, *Journal of Glaciology*, *58*(209), doi:10.3189/2012JoG11J262.

Martin, T., and A. Adcroft (2010), Parameterizing the fresh-water flux from land ice to ocean with interactive icebergs in a coupled climate model, *Ocean Modelling*, *34*, 111–124, doi:10.1016/j.ocemod.2010.05.001.

Mazur, A. K., A. K. Wåhlin, and O. Kalen (2019), The life cycle of small- to medium-sized icebergs in the Amundsen sea embayment, *Polar Research*, *38*(3313), doi:10.33265/polar.v38.3313.

Miles, B. W. J., C. R. Stokes, A. Jenkins, J. R. Jordan, S. S. R. Jamieson, and G. H. Gudmundsson (2020), Intermittent structural weakening and acceleration of the Thwaites Glacier Tongue between 2000 and 2018, *J. Glaciology*, *66*(257), 485–495, doi:10.1017/jog.2020.20.

Milillo, P., E. Rignot, P. Rizzoli, B. Scheuchl, J. Mouginot, J. Bueso-Bello, and P. Prats-Iraola (2019), Heterogeneous retreat and ice melt of Thwaites Glacier, west Antarctica, *Science Advances*, *5*(1), doi:10.1126/sciadv.aau3433.

Morlighem, M. (2020), MEaSUREs BedMachine Antarctica, version 2020-10-08, accessed 2020-10-08, Boulder, Colorado USA. NASA National Snow and Ice Data Center Distributed Active Archive Center, doi:10.5067/E1QL9HFQ7A8M.

Nakayama, Y., R. Timmermann, M. Schroder, and H. H. Hellmer (2014), On the difficulty of modeling Circumpolar Deep Water intrusions onto the Amundsen Sea continental shelf, *Ocean Modelling*, *84*, 26–34, doi:10.1016/j.ocemod.2014.09.007.

Naughten, K. A., P. R. Holland, P. Dutrieux, D. T. Bett, and A. Jenkins (2022), Simulated twentieth-century ocean warming in the Amundsen Sea, west Antarctica, *Geophys. Res. Lett.*, *49*(e2021GL094566), doi:10.1029/2021GL094566.

Ou, H. W. (1991), Some effects of a seamount on oceanic flows, *J. Phys. Oceanogr.*, *21*, 1835–1845.

Padman, L., H. A. Fricker, R. Coleman, S. Howard, and L. Erofeeva (2002), A new tide model for the Antarctic ice shelves and seas, *Annals of Glaciology*, *34*.

Pritchard, H. D., S. R. Ligtenberg, H. A. Fricker, D. G. Vaughan, M. R. van den Broeke, and L. Padman (2012), Antarctic ice-sheet loss driven by basal melting of ice shelves, *Nature*, *484*, 502–505, doi:10.1038/nature10968.

Randall-Goodwin, E., M. P. Meredith, A. Jenkins, P. L. Yager, R. M. Sherrell, E. P. Abrahamsen, R. Guerrero, X. Yuan, R. A. Mortlock, K. Gavahan, A. C. Alderkamp, H. Ducklow, R. Robertson, and S. E. Stammerjohn (2015), Freshwater distributions and water mass structure in the Amundsen Sea Polynya region, Antarctica, *Elem. Sci. Anthropocene*, *3*(65), doi:10.12952/journal.elementa.000065.

Rignot, E., S. Jacobs, J. Mouginot, and B. Scheuchl (2013), Ice-shelf melting around Antarctica, *Science*, *341*, 266–270, doi:10.1126/science.1235798.

Rignot, E., J. Mouginot, B. Scheuchl, M. van der Broeke, M. J. van Wessem, and M. Morlighem (2019), Four decades of Antarctic ice sheet mass balance from 1979–2017, *Proc. Natl. Acad. Sci.*, *116*(4), 1095–1103, doi:10.1073/pnas.1812883116.

Scambos, T., B. Wallin, and J. Bohlander (2022), Images of Antarctic ice shelves, version 2, accessed 16 february 2023, subset 2001–2022 used, Boulder, Colorado USA. NASA National Snow and Ice Data Center Distributed Active Archive Center, doi:10.5067/W87VCY3CW0MJ.

Shchepetkin, A. F., and J. C. McWilliams (2003), A method for computing horizontal pressure-gradient force in an oceanic model with a nonaligned vertical coordinate, *J. Geophys. Res.: Oceans*, *108*(C3), doi:10.1029/2001JC001047.

Shchepetkin, A. F., and J. C. McWilliams (2005), The Regional Oceanic Modeling System (ROMS): A split-explicit, free-surface, topography-following-coordinate oceanic model, *Ocean Model.*, *9*, 347–404, doi:10.1016/j.ocemod.2004.08.002.

Silvano, A., P. R. Holland, K. A. Naughten, O. Dragomir, P. Dutrieux, A. Jenkins, Y. Si, A. L. Stewart, B. P. Molino, G. W. Janzing, T. S. Dotto, and A. C. N. Garabato (2022), Baroclinic ocean response to climate forcing regulates decadal variability of ice-shelf melting in the Amundsen Sea, *Geophys. Res. Lett.*, *49*(e2022GL100646), doi:10.1029/2022GL100646.

St-Laurent, P. (2023), Dataset: A numerical simulation of the ocean, sea ice and ice shelves in the Amundsen Sea (Antarctica) over the period 2006-2022 and its associated code and input files (size 2.2 terabytes), doi:10.25773/bt54-sj65.

St-Laurent, P., P. L. Yager, R. M. Sherrell, S. E. Stammerjohn, and M. S. Dinniman (2017), Pathways and supply of dissolved iron in the Amundsen Sea (Antarctica), *J. Geophys. Res. Oceans*, *122*(9), 7135–7162, doi:10.1002/2017jc013162.

St-Laurent, P., S. E. Stammerjohn, T. Maksym, and R. M. Sherrell (2022), On the relative importance of off-shelf/onshelf drivers of variability in mCDW inventory on the Amundsen shelf, Antarctica, doi:https://doi.org/10.25773/chnp-gd30, https://doi.org/10.25773/chnp-gd30.

St-Laurent, P., S. Stammerjohn, and T. Maksym (2024), Numerical experiments examining the response of onshore oceanic heat supply to yearly changes in the Amundsen Sea icescape (Antarctica), doi:10.17882/99231.

Stammerjohn, S. E., T. Maksym, R. A. Massom, K. E. Lowry, K. R. Arrigo, X. Yuan, M. Raphael, E. Randall-Goodwin, R. M. Sherrell, and P. L. Yager (2015), Seasonal sea ice changes in the Amundsen Sea, Antarctica, over the period of 1979–2014, *Elem. Sci. Anthropocene*, *3*(55), doi:10.12952/journal.elementa.000055.

Thoma, M., A. Jenkins, D. Holland, and S. Jacobs (2008), Modelling Circumpolar Deep Water intrusions on the Amundsen Sea continental shelf, Antarctica, *Geophys. Res. Lett.*, *35*(L18602), doi:10.1029/2008GL034939.

Thurnherr, A. M., S. S. Jacobs, P. Dutrieux, and C. F. Giulivi (2014), Export and circulation of ice cavity water in Pine Island Bay, West Antarctica, *J. Geophys. Res.*, *119*, 1754–1764, doi:10.1002/2013jc009307.

Tournadre, J., N. Bouhier, F. Girard-Adhuin, and F. Rémy (2016), Antarctic icebergs distributions 1992–2014, *J. Geophys. Res.: Oceans*, *121*, 327–349, doi:10.1002/2015JC011178.

Wåhlin, A. K., A. G. C. Graham, K. A. Hogan, B. Y. Queste, L. Boehme, R. D. Larter, E. C. Pettit, J. Wellner, and K. J. Heywood (2021), Pathways and modification of warm water flowing beneath Thwaites ice shelf, west Antarctica, *Science Advances*, *7*(eabd7254), doi:10.1126/sciadv.abd7254.

Webber, B. G. M., K. J. Heywood, D. P. Stevens, P. Dutrieux, E. P. Abrahamsen, A. Jenkins, S. S. Jacobs, H. K. Ha, S. H. Lee, and T. W. Kim (2017), Mechanisms driving variability in the ocean forcing of Pine Island Glacier, *Nat. Comm.*, *8*(14507), doi:10.1038/ncomms14507.

Yager, P., and R. Sherrell (2019), ASPIRE station data used to develop 1-D and 3-D numerical models from the Nathaniel B. Palmer in the Amundsen Sea from 2010-12-14 through 2011-01-05, doi:10.1575/1912/bco-dmo.765081.1.

Yager, P. L., R. M. Sherrell, S. E. Stammerjohn, A. C. Alderkamp, O. Schofield, E. P. Abrahamsen, K. R. Arrigo, S. Bertilsson, D. L. Garay, R. Guerrero, K. E. Lowry, P.-O. Moksnes, K. Ndungu, A. F. Post, E. Randall-Goodwin, L. Riemann, S. Severmann, S. Thatje, G. L. van Dijken, and S. Wilson (2012), ASPIRE: The Amundsen Sea polynya international research expedition, *Oceanography*, *25*(3), 40–53, doi:10.5670/oceanog.2012.73.

Yager, P. L., R. M. Sherrell, S. E. Stammerjohn, H. W. Ducklow, O. M. Schofield, E. D. Ingall, S. E. Wilson, K. E. Lowry, C. M. Williams, L. Riemann, B. Bertilsson, A. C. Alderkamp, J. Dinasquet, R. Logares, A. J. Melara, L. Q. Mu, R. G. Newstead, A. F. Post, R. Swalethorp, and G. L. van Dijken (2016), A carbon budget for the Amundsen Sea Polynya, Antarctica: Estimating net community production and export in a highly productive polar ecosystem, *Elem. Sci. Anthropocene*, *4*(140), doi:10.12952/journal.elementa.000140.

Yang, H. W., T. W. Kim, P. Dutrieux, A. K. Wåhlin, A. Jenkins, H. K. Ha, C. S. Kim, K. H. Cho, T. Park, S. H. Lee, and Y. K. Cho (2022), Seasonal variability of ocean circulation near the Dotson ice shelf, Antarctica, *Nature Communications*, *13*(1138), doi:10.1038/s41467-022-28751-5.

Yoon, S. T., W. S. Lee, S. Nam, C. K. Lee, S. Yun, K. Heywood, L. Boehme, Y. Zheng, I. Lee, Y. Choi, A. Jenkins, E. K. Jin, R. Larter, J. Wellner, P. Dutrieux, and A. T. Bradley (2022), Ice front retreat reconfigures meltwater-driven gyres modulating ocean heat delivery to an Antarctic ice shelf, *Nature Communications*, *13*(306), doi:10.1038/s41467-022-27968-8.

Zheng, Y., D. P. Stevens, K. J. Heywood, B. G. M. Webber, and B. Y. Queste (2022), Reversal of ocean gyres near ice shelves in the Amundsen Sea caused by the interaction of sea ice and wind, *The Cryosphere*, *16*, 3005–3019, doi:10.5194/tc-16-3005-2022.